

Article

# Pr<sup>3+</sup>-Activated Sr<sub>2</sub>LaF<sub>7</sub> Nanoparticles as a Single-Phase White-Light-Emitting Nanophosphor

Bojana Milićević \*, Aleksandar Ćirić, Katarina Milenković , Zoran Ristić, Jovana Periša, Željka Antić and Miroslav D. Dramićanin \* 

Centre of Excellence for Photoconversion, Vinča Institute of Nuclear Sciences—National Institute of the Republic of Serbia, University of Belgrade, 11000 Belgrade, Serbia; aleksandar.ciric@ff.bg.ac.rs (A.Ć.); katarina.milenkovic@vinca.rs (K.M.); risticz@vin.bg.ac.rs (Z.R.); zeljka.antic@vinca.rs (Ž.A.)

\* Correspondence: bojanam@vinca.rs (B.M.); dramican@vinca.rs (M.D.D.)

**Abstract:** Sr<sub>2</sub>LaF<sub>7</sub>:xPr<sup>3+</sup> ( $x = 0.2, 1, 2, 3, 5, 10,$  and  $25$  mol%) nanophosphors with a cubic Fm3m structure were hydrothermally synthesized, forming nearly spherical nanoparticles with an average diameter of approximately 32 nm. Diffuse reflectance measurement and excitation spectra showed a primary excitation peak of Pr<sup>3+</sup> at 443 nm, corresponding to the ground state to the <sup>3</sup>P<sub>2</sub> level transition. Upon blue light excitation, Pr<sup>3+</sup>-activated Sr<sub>2</sub>LaF<sub>7</sub> nanophosphors showed rich emission structure across the visible region of the spectrum, with blue (~483 nm), green (~525 nm), orange (~600 nm), and red (~640 nm) emissions, blue and orange being the most prominent ones. The relative intensities of these emissions varied with Pr<sup>3+</sup> concentration, leading to tunable emission colors. The chromaticity showed slight variation with the Pr<sup>3+</sup> content ( $0.350 < x < 0.417, 0.374 < y < 0.380$ ), while the CCT value increased from 3118 K to 4901 K as the doping concentration increased. The optimized Sr<sub>2</sub>LaF<sub>7</sub> with 2 mol% Pr<sup>3+</sup> had the most intense emission with correlated color temperature (CCT) of 3628 K, corresponding to the warm white color. The proposed Pr<sup>3+</sup>-doping strategy offers valuable insights into discovering or optimizing single-phase phosphors for white-light-emitting applications.

**Keywords:** nanophosphor; fluorides; photoluminescence; Pr<sup>3+</sup> emission; light-based applications



check for updates

Academic Editor: Zhan'ao Tan

Received: 28 April 2025

Revised: 7 May 2025

Accepted: 8 May 2025

Published: 9 May 2025

**Citation:** Milićević, B.; Ćirić, A.; Milenković, K.; Ristić, Z.; Periša, J.; Antić, Ž.; Dramićanin, M.D. Pr<sup>3+</sup>-Activated Sr<sub>2</sub>LaF<sub>7</sub> Nanoparticles as a Single-Phase White-Light-Emitting Nanophosphor. *Nanomaterials* **2025**, *15*, 717. <https://doi.org/10.3390/nano15100717>

**Copyright:** © 2025 by the authors. Licensee MDPI, Basel, Switzerland. This article is an open access article distributed under the terms and conditions of the Creative Commons Attribution (CC BY) license (<https://creativecommons.org/licenses/by/4.0/>).

## 1. Introduction

In recent decades, researchers have been striving to solve the challenge of achieving stable, high-quality white light in LED devices. Two primary approaches have dominated so far. The first approach combines InGaN blue LED chips with YAG:Ce phosphors; however, insufficient red emission results in a low color rendering index (CRI) and unstable light color owing to sensitivity to processing conditions. The second method utilizes UV or near-UV chips to excite distinct red, green, and blue phosphors, enabling wider spectral output, adjustable CRI, and desirable CCT values. However, this method poses challenges, particularly in the controlled synthesis of these phosphors with uniform particle sizes to prevent agglomeration, which is a complex and time-consuming process. To address these limitations, there has been growing interest in single-phase white-light phosphors, which emit white light from a single host material and offer benefits such as simplified fabrication, reduced production costs, and improved reproducibility. These phosphors encompass a broad spectrum of material hosts, such as fluorides, aluminates, silicates, phosphates, molybdates, and tungstates [1–6].

Preferably, host matrices should (i) exhibit non-hygroscopic behavior to maintain stability in air and aqueous environments, (ii) possess a low phonon frequency to minimize

non-radiative relaxation losses and enhance emission efficiency, and (iii) feature a wide band gap to facilitate allowed electronic transitions of the dopant ions while preventing self-absorption [7]. The oxides' hosts exhibit high phonon frequencies ( $>500\text{ cm}^{-1}$ ) and good chemical stability. Halide materials possess low phonon frequencies ( $\leq 300\text{ cm}^{-1}$ ); however, their hygroscopic nature restricts their practical applications. Fluorides stand apart from other hosts by having a phonon frequency in the intermediate range ( $300\text{--}500\text{ cm}^{-1}$ ), good chemical stability, wide optical transmission range, and anionic conductivity [8].

Notably, luminescence-based materials activated by  $\text{Pr}^{3+}$  ions have a broad range of emissions across the ultraviolet, visible, and infrared spectral regions, arising from interconfigurational  $[\text{Xe}]4f^15d^1 \rightarrow [\text{Xe}]4f^2$  and intraconfigurational  $[\text{Xe}]4f^2 \rightarrow [\text{Xe}]4f^2$  electronic transitions [9,10]. These may occur in any form, such as downconversion, downshifting, scintillation, or upconversion. The energy difference between the  $[\text{Xe}]4f^15d^1$  and  $[\text{Xe}]4f^2$  configurations in free  $\text{Pr}^{3+}$  ions is approximately  $62,000\text{ cm}^{-1}$  [9,11]. However, upon doping into crystals, this energy difference considerably reduces because of the crystal field splitting of the  $[\text{Xe}]4f^15d^1$  configuration. The degree of energy difference reduction varies significantly across host matrices, influenced by factors such as spectroscopic ion charge density, polarizability, metal–ligand distances, and site symmetry around  $\text{Pr}^{3+}$  [11,12].

So far, various  $\text{Pr}^{3+}$ -activated fluoride materials have been investigated, providing valuable insights into their potential applications in lighting, displays, sensing, healthcare, and security. Several studies have shown that  $\text{Pr}^{3+}$ -doped fluorides such as  $\text{LiYF}_4$  [13–16],  $\text{LiGdF}_4$  [17,18],  $\text{LiLuF}_4$  [19],  $\text{BaY}_2\text{F}_8$  [20], and  $\text{KY}_3\text{F}_{10}$  [21] are promising candidates for solid-state lasers due to the effective emissions from  $^3\text{P}_0$  across the visible and near-infrared spectral ranges. Mono-dispersed  $\text{Pr}^{3+}$ -doped  $\beta\text{-NaYF}_4$ , with an absolute sensitivity of  $0.01352\text{ K}^{-1}$  at 300 K, and  $\text{Pr}^{3+}$ -doped  $\text{YF}_3$  exhibiting an absolute sensitivity of  $0.012\text{ K}^{-1}$ , with a temperature resolution reaching 0.5 K, are promising candidates for temperature sensing [22,23]. Recently,  $\text{Pr}^{3+}$ -doped fluoride materials have gained significant attention for antimicrobial applications [24]. In this context, Yang et al. observed X-ray-activated strong UVC persistent luminescence, linked to the  $[\text{Xe}]4f^15d^1 \rightarrow [\text{Xe}]4f^2$  transition of  $\text{Pr}^{3+}$ , upon releasing trapped electrons in the fluoride elpasolite  $\text{Cs}_2\text{NaYF}_6$  as a host, providing new insights into their potential applications for sterilization, disinfection, and more [25]. Furthermore, materials that can convert visible light into UVC, such as  $\text{KCaF}_3:\text{Pr}^{3+}$ ,  $\text{CsCaF}_3:\text{Pr}^{3+}$ ,  $\text{RbCaF}_3:\text{Pr}^{3+}$ , and  $\text{BaYF}_5:\text{Pr}^{3+}$ , show strong potential for use in phototherapy, antimicrobial treatments, and photocatalytic processes [26,27]. In addition,  $\beta\text{-NaYF}_4:\text{Pr}^{3+}$ , a single-phase phosphor, is an excellent candidate for white-light-emitting diodes, demonstrating excellent color stability across temperature variations and a CCT value of 5951 K [28].

The growing interest in nanomaterials has increased the demand for novel compounds with intense emissions and efficient synthesis techniques. Nano-sized, lanthanide-doped mixed metal fluorides,  $\text{M}_2\text{LnF}_7$  (where  $\text{M} = \text{Ca}, \text{Sr}, \text{Ba}$  and  $\text{Ln}^{3+} = \text{Y}, \text{La}, \text{Gd}, \text{Lu}$ ), remain relatively unexplored as phosphors, with only a few studies focusing on  $\text{M}_2\text{LaF}_7$  upconversion nanoparticles [29–31]. In this study, cubic  $\text{Pr}^{3+}$ -activated  $\text{Sr}_2\text{LaF}_7$  ( $\text{Pr}^{3+}$  content: 0.2, 1, 2, 3, 5, 10, and 25 mol%) was synthesized hydrothermally at  $180\text{ }^\circ\text{C}$  for 20 h. The main excitation peak of  $\text{Pr}^{3+}$  occurs at 443 nm, and the strongest emission is achieved with an optimal doping concentration of 2 mol%. In addition, the lifetime–concentration relationships show that increasing  $\text{Pr}^{3+}$  concentration shortens lifetime through enhanced non-radiative pathways. Chromaticity ( $x, y$ ) varies slightly, while CCT increases with  $\text{Pr}^{3+}$ -doping. The luminescent properties of  $\text{Pr}^{3+}$ -activated  $\text{Sr}_2\text{LaF}_7$  nanophosphors have not yet been reported in the literature.

## 2. Materials and Methods

### 2.1. Chemicals

Strontium nitrate ( $\text{Sr}(\text{NO}_3)_2$ , Haverhill, MA, USA, 99%), lanthanum (III) nitrate hexahydrate ( $\text{La}(\text{NO}_3)_3 \cdot 6\text{H}_2\text{O}$ , Alfa Aesar, Haverhill, MA, USA, 99.99%), praseodymium oxide ( $\text{Pr}_6\text{O}_{11}$ , Haverhill, MA, USA, 99.9%), disodium ethylenediaminetetraacetate dihydrate ( $\text{EDTA-2Na}$ ,  $\text{C}_{10}\text{H}_{14}\text{N}_2\text{O}_8\text{Na}_2 \cdot 2\text{H}_2\text{O}$ , Kemika, Zagreb, Croatia, 99%), ammonium fluoride ( $\text{NH}_4\text{F}$ , Alfa Aesar, Haverhill, MA, USA, 98%), 25% ammonium solution ( $\text{NH}_4\text{OH}$ , Fisher, Loughborough, Leicestershire, UK), nitric acid (65%  $\text{HNO}_3$ , Macron fine chemicals, Center Valley, PA, USA), and deionized water were used as starting materials without additional purification.

### 2.2. Synthesis of SLF:Pr

The total of seven samples of Pr-doped  $\text{Sr}_2\text{LaF}_7$ —SLF ( $\text{Sr}_2\text{La}_{1-x}\text{Pr}_x\text{F}_7$ ,  $x = 0.002, 0.01, 0.02, 0.03, 0.05, 0.10$ , and  $0.25$ ) were synthesized hydrothermally using  $\text{Sr}^{2+}$  and  $\text{La}^{3+}$ -nitrates,  $\text{Pr}^{3+/4+}$ -oxide, and  $\text{NH}_4\text{F}$  as precursors and  $\text{EDTA-2Na}$  as a stabilizer (Figure 1). Typically, to produce 0.89 g of the representative sample— $\text{Sr}_2\text{LaF}_7$  doped with 2 mol%  $\text{Pr}^{3+}$ —firstly, a stoichiometric quantity of  $\text{Pr}^{3+/4+}$ -oxide was dissolved in 3 mL of concentrated nitric acid and evaporated until oxide transformed into nitrate at  $120^\circ\text{C}$ . After that, the nitrates were weighed corresponding to the stoichiometric ratio (specifically, 0.8465 g  $\text{Sr}^{2+}$ -nitrate, 0.8487 g  $\text{La}^{3+}$ -nitrate) and dissolved in deionized water (12.5 mL) containing Pr-nitrates under continuous stirring at room temperature for 30 min. The resulting solution was then combined with a transparent solution containing 0.7445 g  $\text{EDTA-2Na}$  in 12.5 mL in water (molar ratio  $\text{EDTA-2Na}:\text{La} = 1:1$ ). Subsequently, a 10 mL aqueous solution containing 0.8889 g of  $\text{NH}_4\text{F}$  (molar ratio  $\text{NH}_4\text{F}:\text{La} = 12:1$ ) was introduced and stirred vigorously for 1 h, resulting in the formation of a white complex. The mixture's pH was modified to about 6 by adding 800  $\mu\text{L}$  of  $\text{NH}_4\text{OH}$ . After being sealed in a 100 mL Teflon-lined autoclave, the solution was heated at  $180^\circ\text{C}$  for 20 h. Upon natural cooling, the products were centrifuged, washed twice with water and once with a 1:1 ethanol/water mixture to remove any remaining residues, and then dried in an air atmosphere at  $80^\circ\text{C}$  for 4 h. SLF phosphors with different  $\text{Pr}^{3+}$  concentrations ( $x = 0.2, 1, 2, 3, 5, 10$ , and 25 mol%) relative to  $\text{La}^{3+}$  ions were synthesized following the procedure outlined above. Table 1 shows the specific precursor quantities used to prepare 0.002 mol of  $\text{Sr}_2\text{La}_{1-x}\text{Pr}_x\text{F}_7$  ( $x = 0.002, 0.01, 0.02, 0.03, 0.05, 0.10$ , and  $0.25$ ) samples.

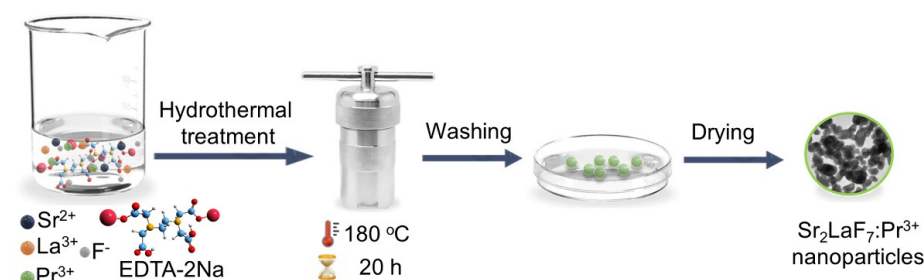


**Figure 1.** Illustration of the synthesis procedure of SLF:Pr nanophosphors via an EDTA-assisted hydrothermal method.

**Table 1.** The specific precursor quantities needed for preparing 0.002 mol of  $\text{Sr}_2\text{La}_{1-x}\text{Pr}_x\text{F}_7$  ( $x = 0.002, 0.01, 0.02, 0.03, 0.05, 0.10$ , and  $0.25$ ).

Molecular Formula	$\text{Pr}^{3+}$ (mol%)	Abbreviated Name	Precursors (g)				
			$\text{Sr}(\text{NO}_3)_2$	$\text{La}(\text{NO}_3)_3 \cdot 6\text{H}_2\text{O}$	$\text{Pr}_6\text{O}_{11}$	$\text{NH}_4\text{F}$	$\text{EDTA-2Na}$
$\text{Sr}_2\text{La}_{0.998}\text{Pr}_{0.002}\text{F}_7$	0.2	SLF:0.2Pr	0.8465	0.8643	0.0007	0.8889	0.7445

Table 1. Cont.

Molecular Formula	Pr <sup>3+</sup> (mol%)	Abbreviated Name	Precursors (g)				
			Sr(NO <sub>3</sub> ) <sub>2</sub>	La(NO <sub>3</sub> ) <sub>3</sub> ·6H <sub>2</sub> O	Pr <sub>6</sub> O <sub>11</sub>	NH <sub>4</sub> F	EDTA-2Na
Sr <sub>2</sub> La <sub>0.99</sub> Pr <sub>0.01</sub> F <sub>7</sub>	1	SLF:1Pr	0.8465	0.8574	0.0034	0.8889	0.7445
Sr <sub>2</sub> La <sub>0.98</sub> Pr <sub>0.02</sub> F <sub>7</sub>	2	SLF:2Pr	0.8465	0.8487	0.0068	0.8889	0.7445
Sr <sub>2</sub> La <sub>0.97</sub> Pr <sub>0.03</sub> F <sub>7</sub>	3	SLF:3Pr	0.8465	0.8401	0.0102	0.8889	0.7445
Sr <sub>2</sub> La <sub>0.95</sub> Pr <sub>0.05</sub> F <sub>7</sub>	5	SLF:5Pr	0.8465	0.82274	0.0170	0.8889	0.7445
Sr <sub>2</sub> La <sub>0.90</sub> Pr <sub>0.10</sub> F <sub>7</sub>	10	SLF:10Pr	0.8465	0.7794	0.0340	0.8889	0.7445
Sr <sub>2</sub> La <sub>0.75</sub> Pr <sub>0.25</sub> F <sub>7</sub>	25	SLF:25Pr	0.8465	0.6495	0.0851	0.8889	0.7445

### 2.3. Characterization

X-ray diffraction (XRD) analysis was conducted using a Rigaku SmartLab system (Tokyo, Japan), employing Cu K $\alpha$  radiation (30 mA, 40 kV) over a 2 $\theta$  range of 10° to 90°. The diffraction data were collected with a step size of 0.02° and a scanning rate of 1°/min across the analyzed 2 $\theta$  range. The microstructure of the samples was examined using a Tecnai GF20 transmission electron microscope (TEM) operating at 200 kV (Hillsboro, OR, USA). ImageJ software (Open-source software, <https://imagej.net/>, accessed on 6 May 2025) was used to determine the average particle size. Diffuse reflectance spectra were obtained using a Shimadzu UV-2600 (Shimadzu Corporation, Tokyo, Japan) spectrophotometer equipped with an ISR-2600 integrated sphere, with BaSO<sub>4</sub> serving as the reference standard. Luminescence measurements were carried out using a 450 nm laser as the excitation source. Emission and excitation spectra were recorded with a Fluorolog-3 Model FL3-221 spectrofluorometer system (Horiba-Jobin-Yvon, Longjumeau, France), utilizing a 450 nm laser for excitation. Excited-state lifetime evaluations were performed using an FHR1000 high-resolution monochromator (Horiba Jobin Yvon), an ICCD camera (Horiba Jobin Yvon 3771, Longjumeau, France), and a 450 nm laser source. Quantum efficiency measurements were performed using a home-built system, consisting of Ocean Insight IDP-REF 38.1 mm integrating sphere fiber coupled to the 450 nm laser light source on the reference port and the OCEAN-FX-XR1-ES extended range spectrometer (Winter Park, FL, USA) on the sample port of the sphere, using BaSO<sub>4</sub> as the standard reference. All data were collected at room temperature.

## 3. Results and Discussion

### 3.1. Structure and Morphology

The M<sub>x</sub>LnF<sub>2x+3</sub> fluorides crystallize in a cubic structure with the Fm3m space group [30]. XRD patterns of Sr<sub>2</sub>La<sub>1-x</sub>Pr<sub>x</sub>F<sub>7</sub> ( $x = 0.002, 0.010, 0.020, 0.030, 0.050, 0.100,$  and  $0.250$ ) nanophosphors with varying Pr<sup>3+</sup> concentrations are shown in Figure 2a. Although Pr<sup>3+</sup> ions were introduced, the main diffraction peaks appearing at approximately 2 $\theta = 26.3, 30.4, 43.7, 51.7, 54.2, 63.5, 70.0, 72.1,$  and  $80.3^\circ$  remained unchanged. These peaks correspond to the 111, 200, 220, 311, 222, 400, 331, 420, and 422 crystal planes, respectively, and show excellent agreement with the standard diffraction data for pure Sr<sub>2</sub>LaF<sub>7</sub>, as documented in ICDD card No. 00–053–0774. The patterns revealed no evidence of additional phases or impurity-related diffraction peaks. The sharp diffraction peaks indicate a good crystallinity of SLF nanophosphors. Table 2 shows the results of the structural analysis: crystallite size (CS), microstrain values, unit cell parameters ( $a$ ), unit cell volume (CV), and the parameters of the data fitting ( $R_{wp}, R_p, R_e, GOF$ ) of SLF: $x$ Pr ( $x = 0.2, 1, 2, 3, 5, 10,$  and  $25$  mol%) nanophosphors.

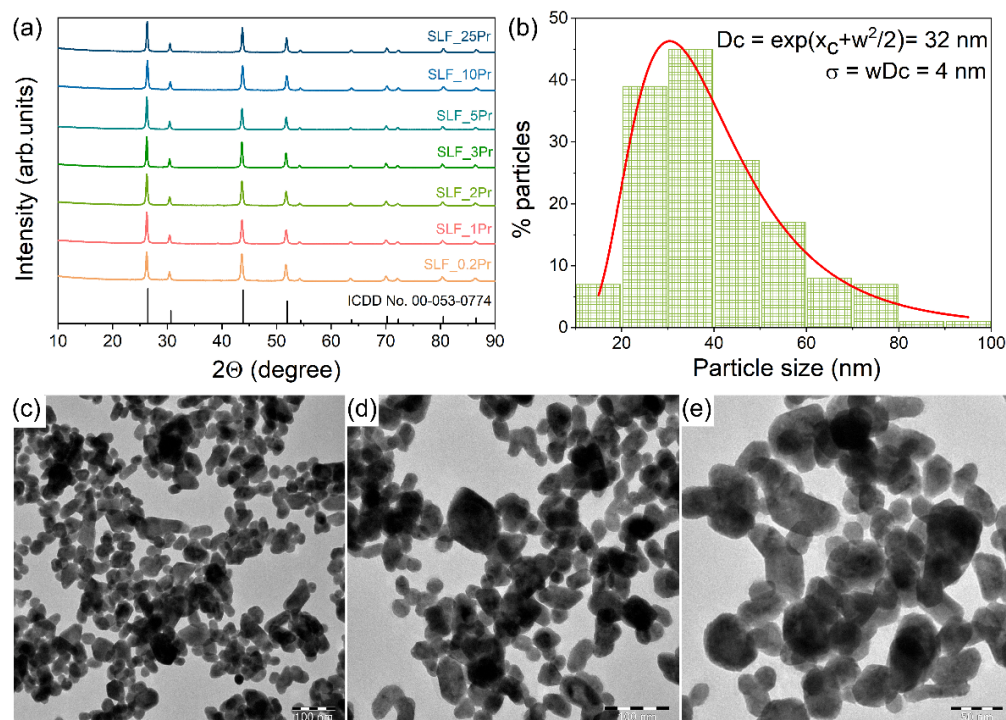


**Figure 2.** (a) XRD patterns of hydrothermally synthesized  $\text{Sr}_2\text{LaF}_7:x\text{Pr}$  ( $x = 0.2, 1, 2, 3, 5, 10,$  and  $25$  mol%) samples presented with the ICDD card No. 00–053–0774 for pure  $\text{Sr}_2\text{LaF}_7$ . (b) Particle size distribution histogram. (c–e) TEM images of the representative SLF:2Pr sample with different magnification  $\times 40,000$ ,  $\times 60,000$ , and  $\times 100,000$ .

**Table 2.** Results of the structural analysis of SLF: $x\text{Pr}$  ( $x = 0.2, 1, 2, 3, 5, 10,$  and  $25$  mol%) nanophosphors.

$\text{Pr}^{3+}$ Content (mol%)	0.2	1	2	3	5	10	25
Abbreviated Name	SLF:0.2Pr	SLF:1Pr	SLF:2Pr	SLF:3Pr	SLF:5Pr	SLF:10Pr	SLF:25Pr
$a = b = c$ (Å)	5.8465 (2)	5.8541 (3)	5.8492 (3)	5.84912 (15)	5.8528 (3)	5.83895 (16)	5.85336 (17)
$CV$ (Å <sup>3</sup> )	199.84 (3)	200.62 (4)	200.12 (4)	200.11 (2)	200.49 (4)	199.07 (2)	200.55 (2)
$CS$ (Å)	185.0 (15)	230.4 (10)	229.9 (2)	268.6 (10)	266.4 (9)	236.80 (8)	293.0 (6)
Strain	0.120 (10)	0.141 (19)	0.146 (4)	0.036 (12)	0.145 (11)	0.1704 (13)	0.124 (6)
GOF	1.4617	1.7782	1.7023	1.6925	2.2436	1.3764	1.3033
* $R_{wp}$	5.37	6.42	6.08	6.26	8.31	5.05	4.90
** $R_p$	4.04	4.65	4.42	4.69	5.89	3.71	3.66
*** $R_e$	3.67	3.61	3.57	3.70	3.70	3.67	3.76

\*  $R_{wp}$ —the weighted profile factor; \*\*  $R_p$ —the profile factor; \*\*\*  $R_e$ —the expected weighted profile factor; GOF—the goodness of fit.

The SLF:Pr nanophosphors were synthesized using an EDTA-assisted hydrothermal method, where EDTA, an effective complexing agent, enhances the dispersibility of crystalline seeds by producing  $[\text{Sr-EDTA}]^{2+}$  and  $[\text{La-EDTA}]^+$  complexes, thus inhibiting the aggregation of SLF particles during the hydrothermal treatment. The resulting morphology and particle size distribution of the representative SLF:2Pr sample, observed at different magnifications, are presented in the TEM images and histogram shown in Figure 2b–e. The nanoparticles exhibit an almost spherical morphology, with an average particle size of approximately  $32 \pm 4$  nm, as estimated from a histogram based on roughly 200 particles and fitted with a log-normal distribution (Figure 2b). High-particle-density zones, which form aggregates and areas with lower dispersed particles, are noticed at lower magnification

(Figure 2c), whereas the variation in particle size and shape can be visualized at higher magnification in Figure 2e.

### 3.2. Photoluminescence Properties of SLF:Pr

$\text{Pr}^{3+}$  ions provide emissions originating from  $4f^5d \rightarrow 4f^2$  and  $4f^2 \rightarrow 4f^2$  electronic transitions that cover the UVC to NIR spectral range. If the lowest-energy  $4f^5d$  level has lower energy than the  $4f^2 \ ^1S_0$  state, the parity-allowed transitions from  $4f^5d$  exhibit UV emission as a dominant one. In the case of fluorides,  $4f^5d$  levels usually have higher energy than the  $^1S_0$  state, which facilitates VIS-NIR emissions from a cascade  $4f^2 \rightarrow 4f^2$  transitions. If  $4f^5d$  and  $^1S_0$  are close in energy, both types of transitions occur.

Figure 3a displays the diffuse reflection spectra of  $\text{Sr}_2\text{LaF}_7:x\text{Pr}$  ( $x = 0.2, 1, 2, 3, 5, 10,$  and  $25$  mol%) nanophosphors recorded at room temperature across the visible wavelength range.  $\text{Pr}^{3+}$  absorptions from  $^3\text{H}_4 \rightarrow ^3\text{P}_{0,1,2} + ^1\text{I}_6$  and  $^3\text{H}_4 \rightarrow ^1\text{D}_2$  transitions are evident in the blue and orange-red spectral areas, with the most intense absorption peak at  $443$  nm attributed to the  $^3\text{H}_4 \rightarrow ^3\text{P}_2$  electronic transition, which is known for its relatively high absorption cross-section [32].

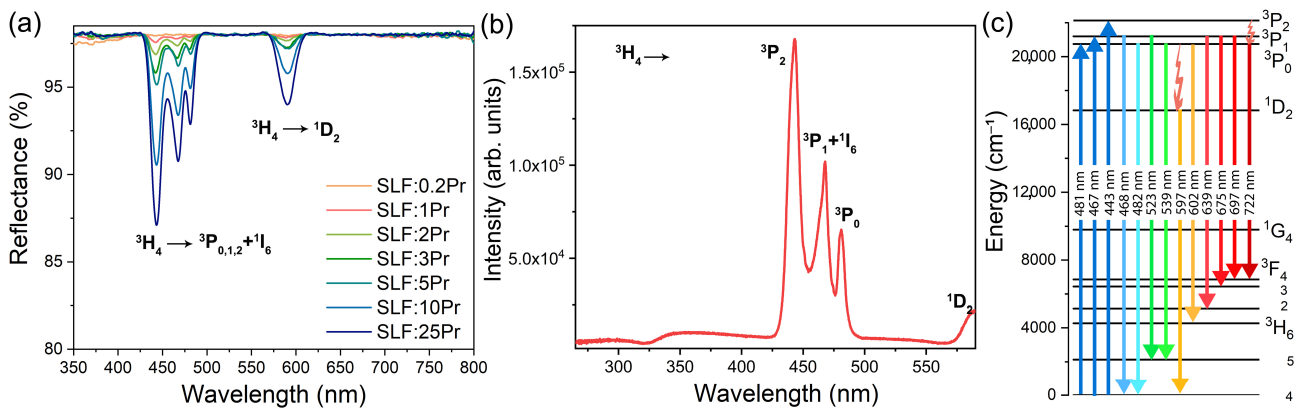


**Figure 3.** (a) Diffuse reflectance spectra of SLF: $x\text{Pr}$  ( $x = 0.2, 1, 2, 3, 5, 10,$  and  $25$  mol%) samples. (b) The excitation spectrum of SLF:2Pr obtained by monitoring  $\lambda_{\text{em}} = 600$  nm. (c) Energy level diagram of the mechanisms of  $\text{Pr}^{3+}$  emission.

Figure 3b shows the excitation spectrum recorded with a  $600$  nm emission wavelength, exhibiting a spectral profile similar to Figure 3a. The primary excitation peak originates from the ground state to the  $^3\text{P}_2$  level of  $\text{Pr}^{3+}$  at  $443$  nm. The  $^3\text{P}_1$  and  $^1\text{I}_6$  levels overlap at  $467$  nm, while the  $^3\text{P}_0$  level appears as the sharpest peak at  $481$  nm due to its  $J = 0$  total angular momentum, which prevents Stark splitting. The excitation into the  $^1\text{D}_2$  level is observed at  $590$  nm. These observations indicate that the  $^3\text{P}_2$ ,  $^3\text{P}_1 + ^1\text{I}_6$ ,  $^3\text{P}_0$ , and  $^1\text{D}_2$  levels are positioned at energies of  $22,573$   $\text{cm}^{-1}$ ,  $21,413$   $\text{cm}^{-1}$ ,  $20,790$   $\text{cm}^{-1}$ , and  $16,949$   $\text{cm}^{-1}$ , respectively (see Figure 3c). The excitation spectrum aligns well with the  $450$  nm laser light used to generate the emissions recorded in Figure 4a. From the  $^3\text{P}_2$  level, the electrons non-radiatively de-excite to the lowest level of the  $^3\text{P}_1$  multiplet by the multiphonon mechanism [33].

The emission spectra feature transitions including  $^3\text{P}_1 \rightarrow ^3\text{H}_4$  at  $468$  nm,  $^3\text{P}_1 \rightarrow ^3\text{H}_4$  at  $483$  nm,  $^3\text{P}_1 \rightarrow ^3\text{H}_5$  at  $525$  nm,  $^3\text{P}_0 \rightarrow ^3\text{H}_5$  at  $539$  nm,  $^1\text{D}_2 \rightarrow ^3\text{H}_4$  at  $597$  nm,  $^3\text{P}_0 \rightarrow ^3\text{H}_6$  at  $602$  nm,  $^3\text{P}_1 \rightarrow ^3\text{F}_2$  at  $640$  nm,  $^3\text{P}_1 \rightarrow ^3\text{F}_3$  at  $675$  nm,  $^3\text{P}_1 \rightarrow ^3\text{F}_4$  at  $697$  nm, and  $^3\text{P}_0 \rightarrow ^3\text{F}_4$  at  $722$  nm, similar to what was reported for other  $\text{Pr}^{3+}$ -doped materials [28,34–38]. Here, the observed emission peaks are broader, which can be attributed to the nanoscale dimensions of the analyzed SLF: $x\text{Pr}$  ( $x = 0.2, 1, 2, 3, 5, 10,$  and  $25$  mol%) particles. The emissions from the  $^3\text{P}_1$  level occur because this level is readily populated at room temperature, owing to its small energy separation from the  $^3\text{P}_0$  level [22]. According to the relation for the fractional

thermal population [39], the percentage of optical centers in  $^3P_1+^1I_6$  levels is about 30% at 300 K. The  $^3P_2$  level lying at about  $1750\text{ cm}^{-1}$  from the  $^3P_0$  level is energetically too far to be significantly populated at room temperature.

The integrated emission intensity (Figure 4b) reveals that 2 mol%  $\text{Pr}^{3+}$ -doping yields the strongest emission, representing the optimal concentration after which concentration quenching begins. Thus, 2 mol% is the optimal doping concentration for the  $\text{Sr}_2\text{LaF}_7$  host by  $\text{Pr}^{3+}$  ions.

The normalized spectra presented in Figure 4c show that as concentration increases, the peak at  $\sim 600\text{ nm}$  diminishes relative to the blue emission. This peak comprises overlapping  $^1D_2$  and  $^3P_0$  emissions, and since the spectra are already normalized to the  $^3P_0$  emissions, this means that there is a decrease in  $^1D_2$  emissions with increasing concentration. This changing emission ratio between  $^1D_2$  and  $^3P_0$  levels stems from non-radiative processes. Higher  $\text{Pr}^{3+}$  concentrations reduce inter-ionic distances, enhancing cross-relaxation mechanisms that preferentially quench the  $^1D_2$  level while affecting  $^3P_0$  emission less [40]. This selective quenching explains the increasing  $I(^3P_0)/I(^1D_2)$  ratio at higher concentrations. This reduction in the red component by suppressing the  $^1D_2$  emission is a pathway for color tunability of this phosphor. For the  $\text{SLF}:\text{Pr}^{3+}$  samples, quantum efficiencies were determined to be 16%, 25%, 55%, 51%, 31%, 20%, and 7% for  $\text{Pr}^{3+}$ -dopant concentrations of 0.2%, 1%, 2%, 3%, 5%, 10%, and 25%, respectively.

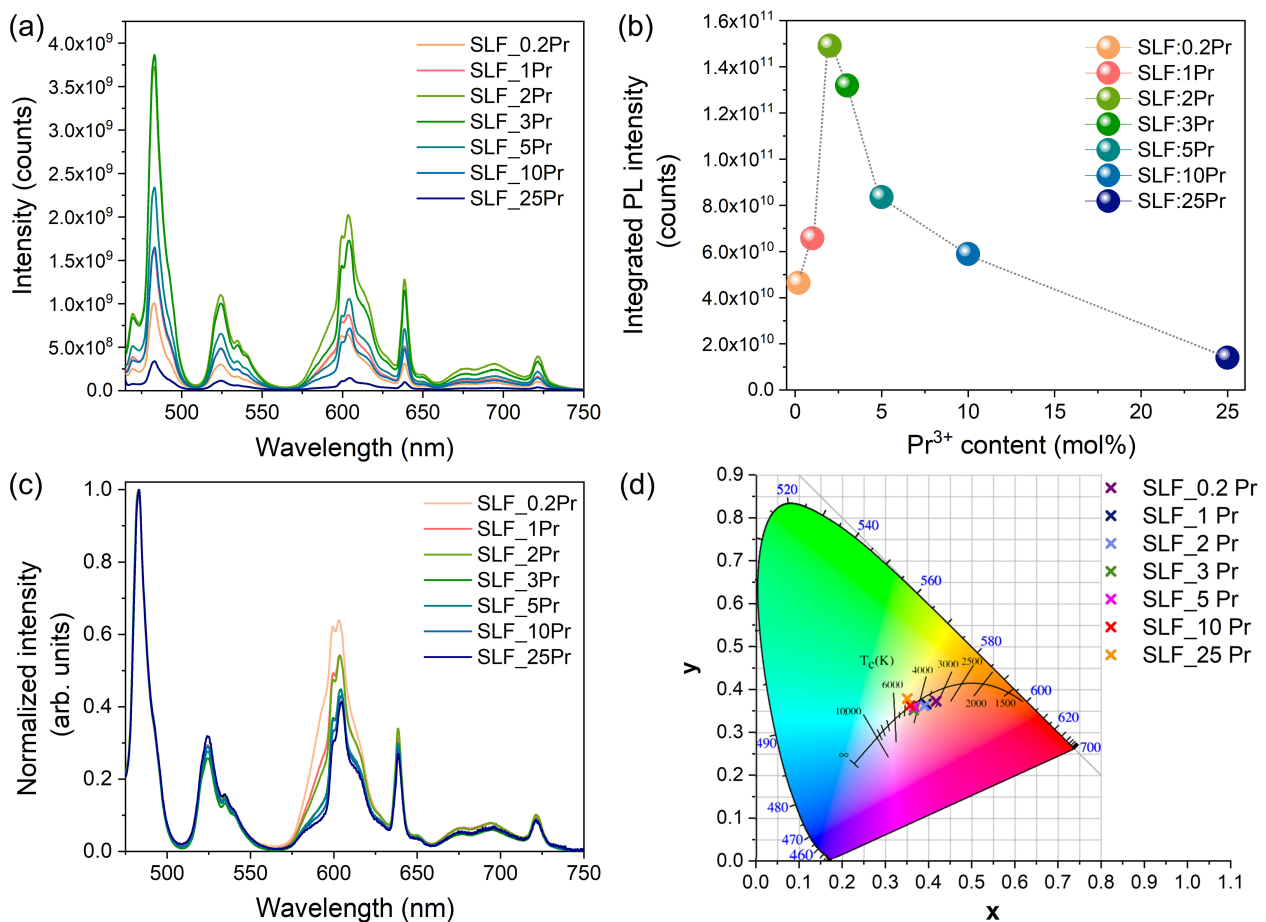


**Figure 4.** (a) Emission spectra after 450 nm laser irradiation and (b) integrated emission intensity as a function of  $\text{Pr}^{3+}$  concentration. (c) Normalized emission spectra. (d) CIE chromaticity diagram of  $\text{SLF}:\text{xPr}$  ( $x = 0.2, 1, 2, 3, 5, 10,$  and  $25\text{ mol}\%$ ) samples obtained from emission spectra in (a). The solid black line represents the Planckian locus, with several color temperatures indicated along it [41].

So far, researchers have typically aimed to design phosphors whose chromaticity values align with the blackbody radiator curve, also known as the Planckian locus. When this is achieved, the light source should match the color temperature of a blackbody at the same physical temperature. However, the concept can still be applied even when a phosphor's chromaticity deviates slightly from the blackbody curve. In such cases, the correlated color temperature (CCT) is used, which represents the temperature of the blackbody radiation that has chromaticity nearly matching that of the source. CCT is a key metric influencing how warm or cool the phosphors' emission appears to human perception. For example, incandescent bulbs, common in homes, emit warm light and typically have CCT values between 2700 and 3000 K [42]. On the other hand, fluorescent lights, which appear cool/daylight white, usually fall within the 4000 to 6000 K range due to the lack of red emission [42]. Figure 4d shows that the chromaticity coordinates of the SLF: $x$ Pr ( $x = 0.2, 1, 2, 3, 5, 10,$  and  $25$  mol%) phosphors are located near the Planckian locus and exhibit minor changes with increasing Pr<sup>3+</sup>-doping concentration. Also, the CCT values given in Table 3 are higher with an increase in Pr<sup>3+</sup>-doping concentration. This is consistent with the increase in the I(<sup>3</sup>P<sub>0</sub>)/I(<sup>1</sup>D<sub>2</sub>) emission intensity ratio. Previous studies on single-phase  $\beta$ -NaYF<sub>4</sub>:Pr<sup>3+</sup> and KYF<sub>4</sub>:Pr<sup>3+</sup> reported the chromaticity coordinates of cool white light with CCT values between 4500 and 6800 K due to the lack of red emission [28,39]. Here, CCT values change with Pr<sup>3+</sup>-doping concentration and range from 3100 to 4900 K. Due to strong red emission, the optimized SLF:2Pr sample emits warm white light at (0.390, 0.363) and a CCT of 3628 K. Our findings are similar to BaY<sub>2</sub>F<sub>8</sub>:Pr<sup>3+</sup> and KY<sub>3</sub>F<sub>10</sub>:Pr<sup>3+</sup> phosphors, as given in Table 3 showing previously reported chromaticity coordinates of white light with CCT values for single-phase white-light-emitting fluoride and results obtained in this work. However, chromaticity values ( $x, y$ ) of optimized SLF:2Pr are much closer to the Planckian locus when compared with BaY<sub>2</sub>F<sub>8</sub>:Pr<sup>3+</sup> and KY<sub>3</sub>F<sub>10</sub>:Pr<sup>3+</sup> phosphors, indicating that its emitted light exhibits a color most similar to natural warm white light.

**Table 3.** Colorimetric parameters of Sr<sub>2</sub>LaF<sub>7</sub>: $x$ Pr ( $x = 0.2, 1, 2, 3, 5, 10,$  and  $25$  mol%) and previously reported Pr<sup>3+</sup>-activated single-phase white-light-emitting phosphors.

Sample	Pr <sup>3+</sup> Content (%)	$\lambda_{\text{exc}}$ (nm)	( $x, y$ )	CCT (K)	Reference
$\beta$ -NaYF <sub>4</sub> :Pr <sup>3+</sup>	0.1	443	(0.354, 0.339)	4563	[28]
	0.5		(0.323, 0.338)	5951	
	1.0		(0.307, 0.335)	6767	
BaY <sub>2</sub> F <sub>8</sub> :Pr <sup>3+</sup>	0.3	457.9	(0.35, 0.32)	4667	[36]
	1.25		(0.38, 0.34)	3724	
	3.0		(0.40, 0.34)	3158	
KYF <sub>4</sub> :Pr <sup>3+</sup>	1.25	457.9	(0.35, 0.31)	4604	[36]
KY <sub>3</sub> F <sub>10</sub> :Pr <sup>3+</sup>	0.3	457.9	(0.37, 0.32)	3861	[36]
Sr <sub>2</sub> LaF <sub>7</sub> :Pr <sup>3+</sup>	0.2	468	(0.417, 0.374)	3105	This work
	1		(0.394, 0.367)	3561	
	2		(0.390, 0.363)	3628	
	3		(0.365, 0.353)	4292	
	5		(0.366, 0.360)	4308	
	10		(0.357, 0.364)	4628	
	25		(0.350, 0.380)	4924	

According to its excitation spectrum, SLF: $x$ Pr ( $x = 0.2, 1, 2, 3, 5, 10,$  and  $25$  mol%) phosphor is an excellent candidate for light-based applications using commercially available,

cost-effective, and powerful blue chips, particularly those operating at 470 nm. Knowing that the LED output light consists of a tunable ratio of LED chip light and phosphor emission [43], it is possible to tune LED emission from cool/daylight white (4000–6000 K) to warm white (2700–3000 K) by choosing the  $\text{Pr}^{3+}$  content in the SLF phosphor.

Figure 5a–c displays the temporal dependence of  $\text{Pr}^{3+}$  luminescence for  $^3\text{P}_{0,1}$  levels ( $\tau_1$ , 530–550 nm), the  $^1\text{D}_2$  level ( $\tau_2$ , 579–593 nm), and overlapping  $^1\text{D}_2$  and  $^3\text{P}_0$  levels ( $\tau_3$ , 601–620 nm), with corresponding lifetime–concentration relationships shown in Figure 5d. The thermalized  $^3\text{P}_{0,1}$  levels share identical lifetimes. The lifetime values ( $\tau$ ) were calculated by fitting the data to normalized intensity decay curves with a single exponential model (Equation (1)):

$$I(t) = I_0 e^{-\frac{t}{\tau}} \quad (1)$$

where  $I(t)$  represents the corresponding emission intensity at time  $t$ ,  $I_0$  represents the corresponding emission intensity at time  $t = 0$  (ideally  $I_0 = 1$  for normalized  $I(t)$ ), and  $\tau$  represents the emission decay constant (excited-state lifetime). Fitting parameters are shown in Table 4 for all the samples in all three wavelength ranges, resulting in goodness-of-fit parameters ( $R^2$ ) being above 0.99 for all except for SLF:25Pr, where the lifetime values are approximate and serve a phenomenological role to illustrate the impact of concentration quenching.

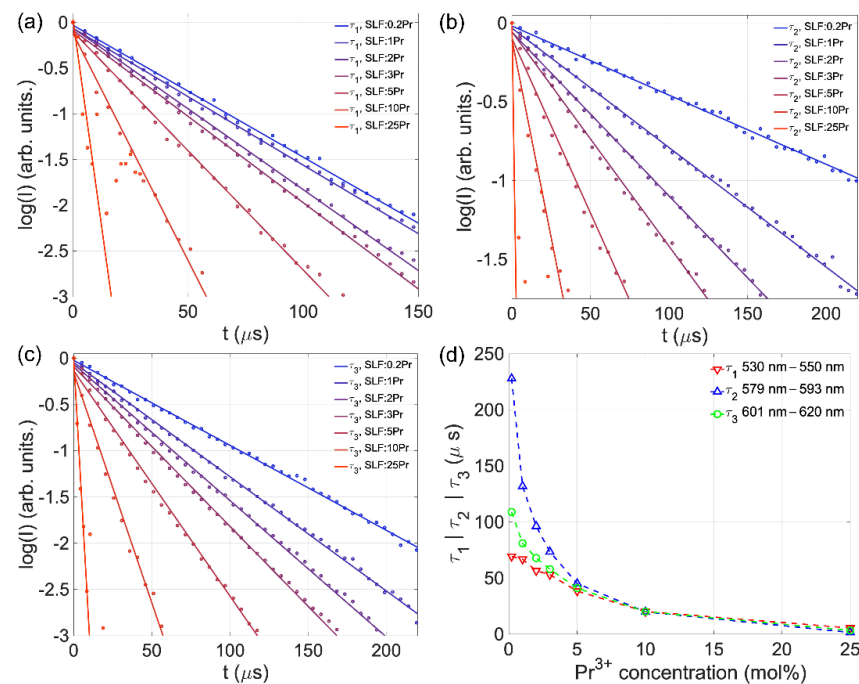


**Figure 5.** Emission decay curves for (a)  $^3\text{P}_{0,1}$  levels ( $\tau_1$ , 530–550 nm), (b)  $^1\text{D}_2$  level ( $\tau_2$ , 579–593 nm), and (c) overlapping  $^1\text{D}_2$  and  $^3\text{P}_0$  levels ( $\tau_3$ , 601–620 nm). (d) Lifetime value vs.  $\text{Pr}^{3+}$  concentration in SLF.

The lifetimes of both  $^3\text{P}_0$  and  $^1\text{D}_2$  levels uniformly decrease with higher  $\text{Pr}^{3+}$  concentrations, as a result of cross-relaxation effects. At lower  $\text{Pr}^{3+}$  concentrations, the  $^1\text{D}_2$  emission decays more slowly than  $^3\text{P}_0$  due to its greater isolation from the next lower level, resulting in less probable multiphonon relaxation. Increasing concentration then shortens all lifetimes through enhanced cross-relaxation non-radiative pathways. The lifetime changes align with the spectral shape variations observed in Figure 5d:  $^1\text{D}_2$  lifetime decreases more rapidly with concentration than  $^3\text{P}_0$ , with both reaching equivalence at 10 mol%. Thus, the lifetime analysis confirms that the cross-relaxation pathways affect the  $^1\text{D}_2$  population more than that of the  $^3\text{P}_0$  level.

**Table 4.** Fitting parameters from Equation (1) for 530–550 nm ( $\tau_1$ ,  $^3P_{0,1}$  levels), 579–593 nm ( $\tau_2$ ,  $^1D_2$  level), and 601–620 nm ( $\tau_3$ , overlapping  $^1D_2$  and  $^3P_0$  levels) ranges.

Sample	Fitting Parameters					
	$I_{0,1}$	$\tau_1$ [ $\mu$ s]	$I_{0,2}$	$\tau_2$ [ $\mu$ s]	$I_{0,3}$	$\tau_3$ [ $\mu$ s]
SLF:0.2Pr	0.969	69.3	0.981	227.9	0.976	108.9
SLF:1Pr	0.938	66.8	0.968	131.9	0.953	81.0
SLF:2Pr	0.940	56.6	0.943	96.2	0.936	67.8
SLF:3Pr	0.919	53.0	0.945	73.4	0.911	57.9
SLF:5Pr	0.904	38.3	0.905	45.1	0.871	41.0
SLF:10Pr	0.887	20.1	0.898	19.9	0.853	20.1
SLF:25Pr	1.035	5.5	0.984	1.5	0.974	3.4

#### 4. Conclusions

We have successfully fabricated Pr<sup>3+</sup>-doped Sr<sub>2</sub>LaF<sub>7</sub> nanophosphors using a hydrothermal approach, achieving a cubic crystal structure and quasi-spherical particle shape of around 32 nm. We have analyzed photoluminescent properties in detail and demonstrated the following:

(i) Sr<sub>2</sub>LaF<sub>7</sub>:Pr nanophosphors exhibit a prominent blue emission at 483 nm, along with additional green, orange, and red emissions.

(ii) The optimal concentration was observed in Sr<sub>2</sub>La<sub>0.08</sub>Pr<sub>0.02</sub>F<sub>7</sub>, which exhibited the strongest emission and a CCT value of 3628 K.

(iii) The analysis of emission lifetimes showed that increasing the Pr<sup>3+</sup> concentration shortened the lifetimes at all emission wavelengths, particularly for the  $^1D_2$  state, which was more susceptible to concentration-induced quenching than the  $^3P_0$  state.

These findings underscore the potential of SLF:Pr nanophosphors as a single-phase phosphor and their possible use in white LEDs when paired with commercially available, cost-effective blue chips operating at 470 nm. Our future research efforts will be directed toward fabrication and thorough examination of Pr<sup>3+</sup>-activated single-phase microcrystals, with a primary focus on determining their efficiency, temperature stability, and LED fabrication.

**Author Contributions:** Conceptualization, B.M. and M.D.D.; Methodology, A.Ć. and M.D.D.; Formal analysis, A.Ć., J.P. and Ž.A.; Investigation, B.M., K.M., Z.R. and Ž.A.; Data curation, A.Ć., K.M., Z.R. and J.P.; Writing—original draft, B.M. and Ž.A.; Writing—review & editing, M.D.D.; Visualization, Z.R. and J.P.; Supervision, B.M. and M.D.D. All authors have read and agreed to the published version of the manuscript.

**Funding:** This research was supported by the Science Fund of the Republic of Serbia, #GRANT No 10412, LED technology based on bismuth-sensitized Eu<sup>3+</sup> luminescence for cost-effective indoor plant growth—LEDTECH-GROW (Authors: B. Milićević, A. Ćirić, K. Milenković, and J. Periša). Authors from Vinča Institute would like to acknowledge funding from the Ministry of Science, Technological Development, and Innovation of the Republic of Serbia under contract 451-03-136/2025-03/200017.

**Data Availability Statement:** The original contributions presented in the study are included in the article, further inquiries can be directed to the corresponding author.

**Conflicts of Interest:** The authors declare no conflicts of interest.

#### References

1. Pathak, S.; Sakai, N.; Wisnivesky Rocca Rivarola, F.; Stranks, S.D.; Liu, J.; Eperon, G.E.; Ducati, C.; Wojciechowski, K.; Griffiths, J.T.; Haghighirad, A.A.; et al. Perovskite Crystals for Tunable White Light Emission. *Chem. Mater.* **2015**, *27*, 8066–8075. [[CrossRef](#)]

2. Xia, Z.; Meijerink, A. Ce<sup>3+</sup>-Doped Garnet Phosphors: Composition Modification, Luminescence Properties and Applications. *Chem. Soc. Rev.* **2017**, *46*, 275–299. [[CrossRef](#)] [[PubMed](#)]
3. Li, X.; Milićević, B.; Dramićanin, M.D.; Jing, X.; Tang, Q.; Shi, J.; Wu, M. Eu<sup>3+</sup>-Activated Sr<sub>3</sub>ZnTa<sub>2</sub>O<sub>9</sub> Single-Component White Light Phosphors: Emission Intensity Enhancement and Color Rendering Improvement. *J. Mater. Chem. C* **2019**, *7*, 2596–2603. [[CrossRef](#)]
4. Li, G.; Tian, Y.; Zhao, Y.; Lin, J. Recent Progress in Luminescence Tuning of Ce<sup>3+</sup> and Eu<sup>2+</sup>-Activated Phosphors for Pc-WLEDs. *Chem. Soc. Rev.* **2015**, *44*, 8688–8713. [[CrossRef](#)]
5. Shang, M.; Li, C.; Lin, J. How to Produce White Light in a Single-Phase Host? *Chem. Soc. Rev.* **2014**, *43*, 1372–1386. [[CrossRef](#)]
6. Haider, G.; Usman, M.; Chen, T.-P.; Perumal, P.; Lu, K.-L.; Chen, Y.-F. Electrically Driven White Light Emission from Intrinsic Metal–Organic Framework. *ACS Nano* **2016**, *10*, 8366–8375. [[CrossRef](#)]
7. Weber, M.J. *CRC Handbook of Laser Science and Technology, Volume 3, Optical Materials: Part 1*; CRC Press: Boca Raton, FL, USA, 1986; ISBN 0-8493-3512-4.
8. Alain Tressaud, K.R.P. (Ed.) *Photonic and Electronic Properties of Fluoride Materials*, 1st ed.; Elsevier: Amsterdam, The Netherlands, 2016; ISBN 9780128016398.
9. Srivastava, A.M. Aspects of Pr<sup>3+</sup> Luminescence in Solids. *J. Lumin.* **2016**, *169*, 445–449. [[CrossRef](#)]
10. Srivastava, A.M. Inter- and Intraconfigurational Optical Transitions of the Pr<sup>3+</sup> Ion for Application in Lighting and Scintillator Technologies. *J. Lumin.* **2009**, *129*, 1419–1421. [[CrossRef](#)]
11. Antić, Ž.; Racu, A.V.; Medić, M.; Alodhayb, A.N.; Kuzman, S.; Brik, M.G.; Dramićanin, M.D. Concentration and Temperature Dependence of Pr<sup>3+</sup> F-f Emissions in La(PO<sub>3</sub>)<sub>3</sub>. *Opt. Mater.* **2024**, *150*, 115226. [[CrossRef](#)]
12. Zdeb, P.; Rebrova, N.; Lisiecki, R.; Dereń, P.J. Luminescence Properties of an Orthorhombic KLaF<sub>4</sub> Phosphor Doped with Pr<sup>3+</sup> Ions under Vacuum Ultraviolet and Visible Excitation. *Materials* **2024**, *17*, 1410. [[CrossRef](#)]
13. Liu, Z.; Cai, Z.; Huang, S.; Zeng, C.; Meng, Z.; Bu, Y.; Luo, Z.; Xu, B.; Xu, H.; Ye, C.; et al. Diode-Pumped Pr<sup>3+</sup>:LiYF<sub>4</sub> Continuous-Wave Deep Red Laser at 698 Nm. *J. Opt. Soc. Am. B* **2013**, *30*, 302. [[CrossRef](#)]
14. Metz, P.W.; Reichert, F.; Moglia, F.; Müller, S.; Marzahl, D.-T.; Kränkel, C.; Huber, G. High-Power Red, Orange, and Green Pr<sup>3+</sup>:LiYF<sub>4</sub> Lasers. *Opt. Lett.* **2014**, *39*, 3193. [[CrossRef](#)] [[PubMed](#)]
15. Richter, A.; Heumann, E.; Osiac, E.; Huber, G.; Seelert, W.; Diening, A. Diode Pumping of a Continuous-Wave Pr<sup>3+</sup>-Doped LiYF<sub>4</sub> Laser. *Opt. Lett.* **2004**, *29*, 2638. [[CrossRef](#)]
16. Starecki, F.; Bolaños, W.; Braud, A.; Doualan, J.-L.; Basse, G.; Benayad, A.; Nazabal, V.; Xu, B.; Moncorgé, R.; Camy, P. Red and Orange Pr<sup>3+</sup>:LiYF<sub>4</sub> Planar Waveguide Laser. *Opt. Lett.* **2013**, *38*, 455. [[CrossRef](#)] [[PubMed](#)]
17. Li, B.; Li, Y.; Hu, Z.; Du, Z. Tunable Orthogonal Polarized Dual-Wavelength Pr<sup>3+</sup>:LiGdF<sub>4</sub> Lasers in the Visible Range. *J. Russ. Laser Res.* **2024**, *45*, 319–326. [[CrossRef](#)]
18. Bai, J.; Fu, X. Red and Green Dual-Wavelength Pr:LiGdF<sub>4</sub> Laser with a Single Birefringent Filter. *Laser Phys.* **2023**, *33*, 125001. [[CrossRef](#)]
19. Baiocco, D.; Lopez-Quintas, I.; Vázquez de Aldana, J.R.; Tonelli, M.; Tredicucci, A. High Efficiency Diode-Pumped Pr:LiLuF<sub>4</sub> Visible Lasers in Femtosecond-Laser-Written Waveguides. *Opt. Express* **2024**, *32*, 9767. [[CrossRef](#)]
20. Pabœuf, D.; Mhibik, O.; Bretenaker, F.; Goldner, P.; Parisi, D.; Tonelli, M. Diode-Pumped Pr:BaY<sub>2</sub>F<sub>8</sub> Continuous-Wave Orange Laser. *Opt. Lett.* **2011**, *36*, 280. [[CrossRef](#)]
21. Metz, P.W.; Müller, S.; Reichert, F.; Marzahl, D.-T.; Moglia, F.; Kränkel, C.; Huber, G. Wide Wavelength Tunability and Green Laser Operation of Diode-Pumped Pr<sup>3+</sup>:KY<sub>3</sub>F<sub>10</sub>. *Opt. Express* **2013**, *21*, 31274. [[CrossRef](#)]
22. Zhou, S.; Jiang, G.; Wei, X.; Duan, C.; Chen, Y.; Yin, M. Pr<sup>3+</sup>-Doped β-NaYF<sub>4</sub> for Temperature Sensing with Fluorescence Intensity Ratio Technique. *J. Nanosci. Nanotechnol.* **2014**, *14*, 3739–3742. [[CrossRef](#)]
23. Rajčić, A.; Ristić, Z.; Periša, J.; Milićević, B.; Aldawood, S.; Alodhayb, A.N.; Antić, Ž.; Dramićanin, M.D. Using Principal Component Analysis for Temperature Readings from YF<sub>3</sub>:Pr<sup>3+</sup> Luminescence. *Technologies* **2024**, *12*, 131. [[CrossRef](#)]
24. Dramićanin, M.D.; Brik, M.G.; Antić, Ž.; Bănică, R.; Mosoarca, C.; Dramićanin, T.; Ristić, Z.; Dima, G.D.; Förster, T.; Suta, M. Pr<sup>3+</sup> Visible to Ultraviolet Upconversion for Antimicrobial Applications. *Nanomaterials* **2025**, *15*, 562. [[CrossRef](#)] [[PubMed](#)]
25. Yang, Y.-M.; Li, Z.-Y.; Zhang, J.-Y.; Lu, Y.; Guo, S.-Q.; Zhao, Q.; Wang, X.; Yong, Z.-J.; Li, H.; Ma, J.-P.; et al. X-Ray-Activated Long Persistent Phosphors Featuring Strong UVC Afterglow Emissions. *Light Sci. Appl.* **2018**, *7*, 88. [[CrossRef](#)]
26. Rebrova, N.; Grippa, A.; Zdeb, P.; Dereń, P.J. Blue to UV Upconversion Properties of Pr<sup>3+</sup> Doped ACaF<sub>3</sub> (A = K, Rb, Cs) Phosphors. *Scr. Mater.* **2025**, *255*, 116395. [[CrossRef](#)]
27. Rebrova, N.; Zdeb, P.; Lemański, K.; Macalik, B.; Bezakrovnyi, O.; Dereń, P.J. Upconversion Luminescence Properties of Pr<sup>3+</sup>-Doped BaYF<sub>5</sub> Nanoparticles Prepared by Microwave Hydrothermal Method. *Inorg. Chem.* **2024**, *63*, 3028–3036. [[CrossRef](#)]
28. Wei, T.; Bo, W.; Yan, C.; Yeqing, C.; Jun, L.; Qingguang, Z. Single Pr<sup>3+</sup>-Activated High-Color-Stability Fluoride White-Light Phosphor for White-Light-Emitting Diodes. *Opt. Mater. Express* **2019**, *9*, 223. [[CrossRef](#)]
29. Zhao, T.; Hu, L.; Ren, J. Fluorophosphate Upconversion-Luminescent Glass-Ceramics Containing Ba<sub>2</sub>LaF<sub>7</sub>:Er<sup>3+</sup> Nanocrystals: An Advanced Solid-State Nuclear Magnetic Resonance Study. *J. Phys. Chem. C* **2021**, *125*, 26901–26915. [[CrossRef](#)]

30. Grzyb, T.; Przybylska, D. Formation Mechanism, Structural, and Upconversion Properties of Alkaline Rare-Earth Fluoride Nanocrystals Doped with Yb<sup>3+</sup>/Er<sup>3+</sup> Ions. *Inorg. Chem.* **2018**, *57*, 6410–6420. [CrossRef]
31. Mao, Y.; Ma, M.; Gong, L.; Xu, C.; Ren, G.; Yang, Q. Controllable Synthesis and Upconversion Emission of Ultrasmall Near-Monodisperse Lanthanide-Doped Sr<sub>2</sub>LaF<sub>7</sub> Nanocrystals. *J. Alloys Compd.* **2014**, *609*, 262–267. [CrossRef]
32. Malinowski, M.; Wolski, R.; Woliński, W. Spectroscopic Studies of Pr<sup>3+</sup> Ions in KPr<sub>x</sub>Y<sub>1-x</sub>P<sub>4</sub>O<sub>12</sub>. *J. Lumin.* **1986**, *35*, 1–8. [CrossRef]
33. Ćirić, A.; Dramićanin, M.D. LumTHools—Software for Fitting the Temperature Dependence of Luminescence Emission Intensity, Lifetime, Bandshift, and Bandwidth and Luminescence Thermometry and Review of the Theoretical Models. *J. Lumin.* **2022**, *252*, 119413. [CrossRef]
34. Carnall, W.T.; Crosswhite, H.; Crosswhite, H.M. *Energy Level Structure and Transition Probabilities in the Spectra of the Trivalent Lanthanides in LaF<sub>3</sub>*; Argonne National Lab. (ANL): Argonne, IL, USA, 1978.
35. Pawlik, N.; Goryczka, T.; Zubko, M.; Śmiarowska, J.; Pisarski, W.A. White Light and Near-Infrared Emissions of Pr<sup>3+</sup> Ions in SiO<sub>2</sub>-LaF<sub>3</sub> Sol-Gel Nano-Glass-Ceramics. *Nanoscale* **2024**, *16*, 4249–4265. [CrossRef]
36. Toncelli, A.; Bonelli, L.; Faoro, R.; Parisi, D.; Tonelli, M. Investigation of Pr-Doped Fluoride Crystals as Possible White-Light Emitters. *Opt. Mater.* **2009**, *31*, 1205–1209. [CrossRef]
37. Hoa Tran, T.Q.; Hoang, M.H.; Do, T.A.T.; Le, A.T.; Nguyen, T.H.; Nguyen, T.D.; Man, M.T. Nanostructure and Photoluminescence Dynamics of Praseodymium Doped Hexagonal LaF<sub>3</sub> Nanocrystals. *J. Lumin.* **2021**, *237*, 118162. [CrossRef]
38. Jusza, A.; Lipińska, L.; Baran, M.; Olszyna, A.; Jastrzębska, A.; Gil, M.; Mergo, P.; Piramidowicz, R. Praseodymium Doped Nanocrystals and Nanocomposites for Application in White Light Sources. *Opt. Mater.* **2019**, *95*, 109247. [CrossRef]
39. Görller-Walrand, C.; Binnemans, K. Chapter 167 Spectral Intensities of F-f Transitions. In *Handbook on the Physics and Chemistry of Rare Earths*; Elsevier: Amsterdam, The Netherlands, 1998; pp. 101–264.
40. Naresh, V.; Ham, B.S. Influence of Multiphonon and Cross Relaxations on 3P<sub>0</sub> and 1D<sub>2</sub> Emission Levels of Pr<sup>3+</sup> Doped Borosilicate Glasses for Broad Band Signal Amplification. *J. Alloys Compd.* **2016**, *664*, 321–330. [CrossRef]
41. Kunkel, T.; Daly, S.; Miller, S.; Froehlich, J. Perceptual Design for High Dynamic Range Systems. In *High Dynamic Range Video*; Elsevier: Amsterdam, The Netherlands, 2016; pp. 391–430.
42. David, A.; Whitehead, L.A. LED-Based White Light. *Comptes Rendus. Phys.* **2018**, *19*, 169–181. [CrossRef]
43. Available online: [https://www.jstage.jst.go.jp/article/jlve/22/1/22\\_1\\_1\\_2/\\_pdf](https://www.jstage.jst.go.jp/article/jlve/22/1/22_1_1_2/_pdf) (accessed on 1 April 2025).

**Disclaimer/Publisher’s Note:** The statements, opinions and data contained in all publications are solely those of the individual author(s) and contributor(s) and not of MDPI and/or the editor(s). MDPI and/or the editor(s) disclaim responsibility for any injury to people or property resulting from any ideas, methods, instructions or products referred to in the content.